Remote Sensing of Environment 212 (2018) 148–160

Contents lists available at ScienceDirect

Remote Sensing of Environment

journal homepage: www.elsevier.com/locate/rse

Inferring surface currents within submerged, vegetated deltaic islands and wetlands from multi-pass airborne SAR

F. Ayoub[a,b,*], C.E. Jones[b], M.P. Lamb[a], B. Holt[b], J.B. Shaw[c], D. Mohrig[d], W. Wagner[d]

[a] Geological and Planetary Sciences department, California Institute of Technology, Pasadena, CA, USA
[b] Jet Propulsion Laboratory, California Institute of Technology, Pasadena, CA, USA
[c] Department of Geosciences, University of Arkansas, Fayetteville, AR, USA
[d] Jackson School of Geosciences, University of Texas, Austin, TX, USA

ARTICLE INFO

Keywords:
Airborne SAR
Doppler shift
Multi-pass SAR
Water surface current
Wetlands
Delta environment

ABSTRACT

Water flow patterns across coastal and deltaic wetlands affect biogeochemical cycling, denitrification, organic carbon burial, and coastal landscape evolution. Our understanding of such patterns across these important landscapes is incomplete, however, because of the inherent difficulty of conducting spatially and temporally dense ground- or boat-based surveys in shallow, vegetated terrain. We conducted an airborne L-band synthetic aperture radar (SAR) acquisition campaign on Wax Lake Delta, Louisiana, USA, in May 2015, to investigate whether water velocities and flow patterns over kilometer scales can be determined from remote sensing. Thirteen SAR flight lines over the delta region were acquired in 3 h with six different flight directions, concurrently with a small boat campaign. We show that SAR azimuth displacement due to Doppler shift can be used to estimate the surface water flow relative to the static and submerged vegetation interspersed on delta islands, using a simple Bragg wave scattering model and accounting for the Bragg wave's free velocity and wind drift. At Wax Lake Delta, we find that ~0.40 m/s water velocities within the main deltaic channels slow to 0.1–0.2 m/s as flow spreads laterally across, and converges within, the vegetated islands, coinciding with shallow (< 0.5 m) depths and heightened flow resistance. This SAR-based technique opens up new avenues for understanding shallow submerged, vegetated coastal wetlands and deltas.

1. Introduction

Over 300 million people are living on or near river deltas (Syvitski and Saito, 2007). In many of these deltas, land loss due primarily to combined sea level rise and land subsidence threatens their ecological and economic productivity (e.g., Morton and Bernier, 2010; Tessler et al., 2015). Deltas are landforms built and maintained by a complex array of physical, biological, and chemical processes (Galloway, 1975; Orton and Reading, 1993). Flow routing is central to many of these processes because it is coupled to the morphodynamics of landform evolution, the rates of denitrification, and the construction of wetland ecosystems. However, flow routing on deltas is difficult to monitor due to considerable spatial extent and prevalence of very shallow water (< 0.5 m depth), which make both ground and boat surveys difficult. Only sparse in situ stream gage measurements of wetland flow velocities are usually carried out, leaving a major data gap for understanding deltaic wetland hydrology.

Remote sensing techniques can help fill this data gap. For instance, synoptic views and monitoring of vegetation colonization can be obtained from optical spectrometers deployed on satellite and aircraft platforms (Carle et al., 2015). Repeat bathymetry surveys derived from remote sensing can indicate whether a delta is retreating or advancing (Olliver and Edmonds, 2017). However, techniques to survey the bathymetry using optical (visible and laser) imagery can be impeded by water turbidity. Surface currents in a delta could be monitored from ground based High Frequency (HF) radar (Paduan and Rosenfeld, 1996), although large portions can be occluded by emergent vegetation. Air and spaceborne real aperture radar (RAR) and synthetic aperture radar (SAR) imagery have been investigated for the capability to provide coastal bathymetry (de Loor, 1981; Lodge, 1983; Alpers and Hennings, 1984; Romeiser and Alpers, 1997) and current velocities (Lyzenga and Shuchman, 1982; Goldstein et al., 1989), but are generally used in deeper waters and larger ocean channels.

Recent work on the Wax Lake Delta (WLD), a young and shallow river delta prograding in the Atchafalaya Bay, Louisiana, USA, has highlighted both the detailed topography of river deltas, and the complex flow paths across this topography (Shaw and Mohrig, 2014; Kolker et al., 2014; Hiatt and Passalacqua, 2015; Geleynse et al., 2015;

---

* Corresponding author at: MC 169-416, JPL, 4800 Oak Grove Drive, Pasadena, CA 91109, USA.
E-mail address: francois.ayoub@jpl.nasa.gov (F. Ayoub).

https://doi.org/10.1016/j.rse.2018.04.035
Received 4 October 2017; Received in revised form 1 April 2018; Accepted 19 April 2018

Roberts et al., 2015; Shaw et al., 2016a). These remote sensing, modeling and field-based studies have shown that there are strong couplings between bed topography and flow in channels and through the wetlands on islands. Hiatt and Passalacqua (2015) showed that velocities on submerged islands are roughly one third as fast as flow through channels, and found that flow reversals from tides and winds can substantially affect the residence time of water in these islands. Shaw et al. (2016a) used streaklines from biogenic slicks in these regions to estimate flow direction, but could not resolve the flow speed. Synoptic measurements of flow velocity over islands could quantify the residence time of water in islands, an essential parameter in determining denitrification potential (Hiatt and Passalacqua, 2015). Furthermore, the effect of vegetation on flow speeds and patterns is poorly understood (Temmerman et al., 2005), and measurement of flow velocity in deltaic islands is critical to improve understanding of this factor.

In this study, we conducted an airborne field campaign to estimate flow velocities on islands of the WLD using a series of images that we acquired over a 3-h time period with the NASA airborne Uninhabited Aerial Vehicle Synthetic Aperture Radar (UAVSAR) in May 2015. Shaw et al. (2016b) used a similar series of UAVSAR images over the WLD to document morphologic changes of the submerged channels. They compared images acquired over a time span of several years and identified bathymetric change from the change in the SAR backscatter. In this study we specifically investigate the use of airborne SAR imagery to infer the 2-dimensional surface current velocity within a bathymetrically complex, shallow system, including on submerged parts of delta islands. The technique relies upon imaging the delta from multiple directions over tens of minutes, as opposed to Shaw et al. (2016b) which used yearly revisits. Such temporal and geometric constraints require an airborne system because a spaceborne SAR sensor has at most twice-daily overpasses and fixed imaging geometry. We qualitatively compare these derived surface currents with near coincident and adjacent currents derived by boat-based acoustic Doppler current profiler (ADCP) survey. In the following sections we first review background information on SAR-based methods for current estimation. Second, we describe the study area, radar and in situ measurements, and general features of the delta observed with the SAR. Third, we present a theory to derive the 2-D velocity field within shallow submerged vegetation, and apply it flow within a major channel and across the entire delta. Finally, we discuss the measurement uncertainty, errors and limitations.

2. SAR-based methods for current velocity estimation

As generally described by Holt (2004), radar backscatter from the ocean is related to ocean surface roughness components that are of similar scales to the radar wavelength. Because the ocean surface (composed of waves) is moving, it generates Doppler shifts in the radar signal, which can be used to map surface currents, as demonstrated by coastal high-frequency (HF) radars (Paduan and Rosenfeld, 1996) and airborne and spaceborne SAR (e.g., Lyzenga and Shuchman, 1982; Goldstein et al., 1989). In order to determine a current vector, radial velocities of the moving ocean surface must be observed from multiple viewing geometries and combined to form a vector velocity field, which is the technique employed by HF radar networks. A complicating factor is that the Doppler shift from a moving ocean surface can have contributions from multiple moving components including the surface current velocity, wave orbital velocities, and the wave-induced Stokes drift.

Two main techniques have been devised to retrieve the surface current information from SAR imagery. The first technique, called along-track interferometry (ATI), consists of two receiving antennas separated by a sufficiently small distance in the along-track direction to maintain coherent ocean returns (Chapman et al., 1994; Romeiser and Thompson, 2000). The phase difference of the same surface point retrieved from the two complex images is directly related to the displacement of that point during the small delay in acquisition between the two antennas. ATI studies from airborne (e.g. Goldstein and Zebker, 1987; Graber et al., 1996) and spaceborne (Romeiser et al., 2005) platforms have successfully demonstrated the feasibility of the technique, including over rivers (Romeiser et al., 2007). ATI provides the current component in the line-of-sight direction only. To get the full 2D description of the current, ATI must be conducted at different azimuth viewing directions (Goldstein et al., 1989). The second technique relies on the analysis of the Doppler centroid measured from a single receiving antenna and aims at recovering the Doppler shift residual due to the surface current after accounting for the technical details of the satellite or aircraft orbits, the instrument, as well as wave-related parameters and wind (Madsen, 1989; Chapron et al., 2005; Johannessen et al., 2008; Kudryavtsev et al., 2012). This approach requires precise stability and knowledge of the platform track and attitude, which is more readily attainable and accurately measured for spacecraft than aircraft. Similar to ATI, at least two images with different along-track flight directions must be acquired in a short timespan to get the full 2D description of the current, which is impractical for current spaceborne systems.

In this study we develop a technique which is related to the second technique described above, but instead of looking at the Doppler spectra, we use the azimuth displacement, which is a consequence of the Doppler shift effect, to infer the surface current velocity. Our technique involves measuring the azimuth displacement of the moving water with respect to stationary objects in the scene.

3. Study area and SAR survey

3.1. Wax Lake Delta

The WLD was initiated from a channel dredged in 1942 between the Atchafalaya River and the Atchafalaya Bay. The WLD has not undergone engineering modification since and has evolved naturally. The emergent and submerged part of the delta now covers about 150 km^2, with the permanently submerged area extending to 70 km^2 (Allen et al., 2012; Shaw and Mohrig, 2014). The emergent delta consists of a series of islands separated by relatively deep (< 3 m) channels that bifurcate downstream. Downstream of the emergent delta, channels become shallower as the flows they contain lose lateral confinement. Flows across the shallow (< 0.5 m) submerged tops of islands converge into drainage troughs that discharge effluent at positions located between the major distributary channels (Shaw et al., 2016a).

3.2. UAVSAR specifications

UAVSAR is a 1.257 GHz (L-band) SAR polarimetric instrument flown on-board a Gulfstream-3 aircraft operated for the U.S. National Aeronautics and Space Administration (NASA) under its Airborne Science Program (http://uavsar.jpl.nasa.gov/). The instrument is side-looking, imaging to the left of the aircraft heading, and emits and receives in both horizontal (H) and vertical (V) polarizations. The SAR images have a swath width of 22 km and a single-look resolution of 1.7 m in the slant range (line-of-sight) direction and 0.8 m in the along-track direction. The ground range resolution in the cross-track direction is $1.7/\sin(\theta_i)$ m, where θ_i is the incidence angle. UAVSAR has a very low noise floor, less than -50 dB (Fore et al., 2015), which makes it well suited for imaging oceanographic features with low radar backscatter. Other instrument specifications are reported in Table 1.

3.3. Aircraft acquisitions of Wax Lake Delta

On May 8, 2015, we conducted a UAVSAR field campaign to acquire a series of 13 images of WLD with a total of 6 different flight directions. The full time-series acquisition period took 2 h 50 min, with 15–20 min between each acquisition. A SAR image of the WLD is presented in

Table 1
UAVSAR instrument specifications.

Wavelength	0.238 m
Polarization	HH, HV, VV, VH
Flight altitude	12,500 m
Flight speed	220 m/s
Swath	22 km
Look angle	22°–60° (left looking)
Range resolution (single look)	1.7 m
Along-track resolution (single look)	0.8 m

Fig. 1. Water flows out of the apex of the delta ("0" on Fig. 1), spreads in the delta through bifurcated channels, with part of the flow moving onto the islands that serve as sediment depositional areas, and finally flows through the delta front into the bay. A summary of the time-series acquired on May 8, 2015, is presented in Fig. 2 and Table 2, with high resolution images in Supplementary Figures. Images 00, 02, 04, 10, and 12 were acquired from the same flight heading with highly accurate repeat flight tracks such that each ground point was imaged with identical viewing parameters in these five SAR images. The same acquisition conditions apply for images 01, 03, 09 and 11. On the contrary, images 05, 06, 07, and 08 each had single and unique flight headings.

The SAR images were processed at the Jet Propulsion Laboratory, California, and retrieved from the data archive at the Alaska Satellite Facility (https://www.asf.alaska.edu/). The data is delivered in georeferenced format, with a pixel ground resolution of about 5.5 m/pixel after multi-looking (a technique averaging adjacent pixels to reduce speckle noise), and expressed in normalized radar cross section (σ_o). The multi-looking technique, which lowers the speckle noise in the SAR image at the expense of a spatial resolution loss, benefits the subsequent comparison of images by reducing the image correlation noise and outliers. This tradeoff reduced as much noise as possible while keeping a spatial resolution sufficiently high with respect to the scale of processes that need to be monitored. Note also that in this study we entirely worked without the phase information of the SAR images. An ATI-based approach was not possible due to the lifetime and migration speed of the scatters (surface waves) compared to the time span between successive acquisitions, which prevents coherency between the two images (Chapman et al., 1994). All acquisitions have WLD approximately in the midrange of the swath, limiting near and far range effects. The surface backscatter from all the acquisitions of WLD are 10 dB or more above the noise floor. Unless mentioned otherwise, the VV polarization images are used in this study.

3.4. *In situ surface currents*

Concurrent with the SAR acquisitions, a small vessel equipped with a Teledyne acoustic Doppler current profiler (ADCP) measured the water current magnitude and direction along the delta front at an average depth of 1.63 m (0.67 m minimum, 3 m maximum). The post-processing and extraction of the depth-averaged current was done using Teledyne RD Instruments WinRiverII software (http://rdinstruments.com/). Measurement of the surface current closer to the central delta and inside the submerged islands was not possible because of the shallow water depth (< 0.7 m) and presence of dense submerged aquatic vegetation. The acquisition of the current profile took about 5 h, starting on the east side of the delta at approximately 13:00 UTC on May 8, 2015. During the survey the sea state was calm without perceptible swell and mostly small-scale wind waves, with a light breeze from the southeast. For each ADCP profile, the shallowest and the deepest 30 cm were not recorded by the instrument. The current velocity in the intermediate water column was measured with a vertical bin of 20 cm. Investigation of the current velocity profile did not show a significant variation of the current velocity along the measured depth because of the shallow depths. For purposes of qualitative comparison with the remote sensing derived velocities, we assume that the depth-averaged current velocity is a good proxy for the current velocity near the surface ($\overrightarrow{U_c}$ in 5.1).

3.5. *Environmental conditions*

At the time of the SAR acquisitions, the Mississippi River, which feeds the WLD through the Atchafalaya River, was in flood. The water

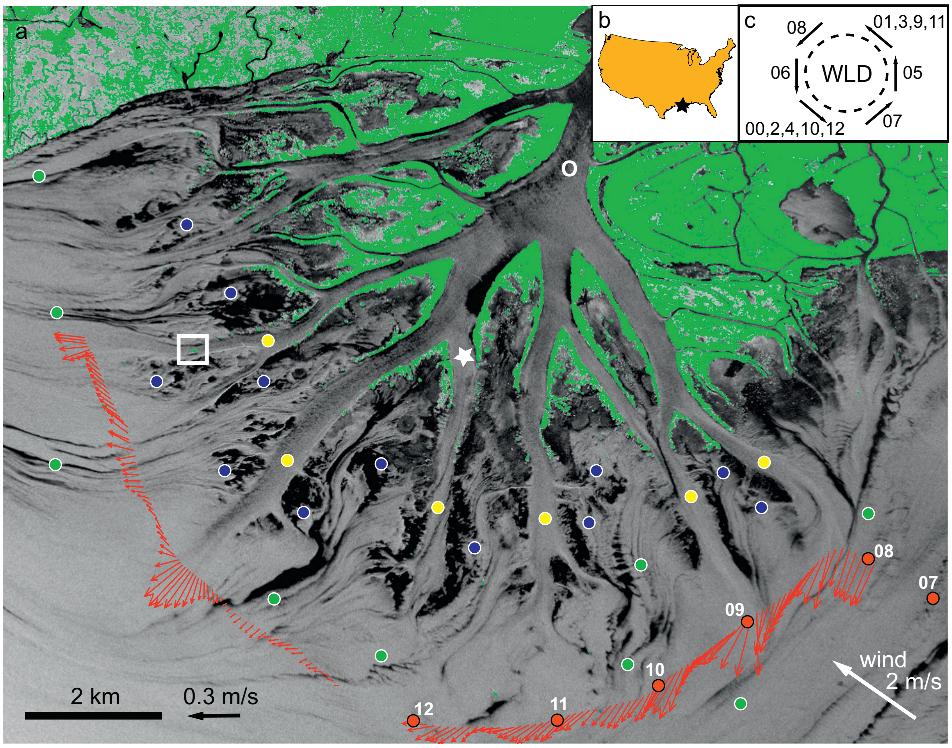

Fig. 1. Wax Lake Delta (WLD) situation and description. a) SAR normalized radar cross section (σ_0) of WLD (short ID 00) acquired on May, 8, 2015. Green indicates emerged vegetation, whereas greyscale indicates water surface. Yellow, blue, and green dots indicate submerged channels, submerged vegetation waves, and biogenic slicks, respectively (blue and green dots are placed on or aside the feature of interest for readability). Red arrows indicate the current velocity measured from the boat-mounted ADCP, acquired on May 08, 2015. Red dots indicate the location of the ADCP boat at the time of some UAVSAR acquisitions (given by the short ID). The star and white box locate Main Pass channel and the oil and gas platform discussed in the text, respectively. b) Location of WLD. c) Flight directions and positions of the UAVSAR aircraft with respect to WLD. Numbers refer to the short ID of the images, listed in Table 2.

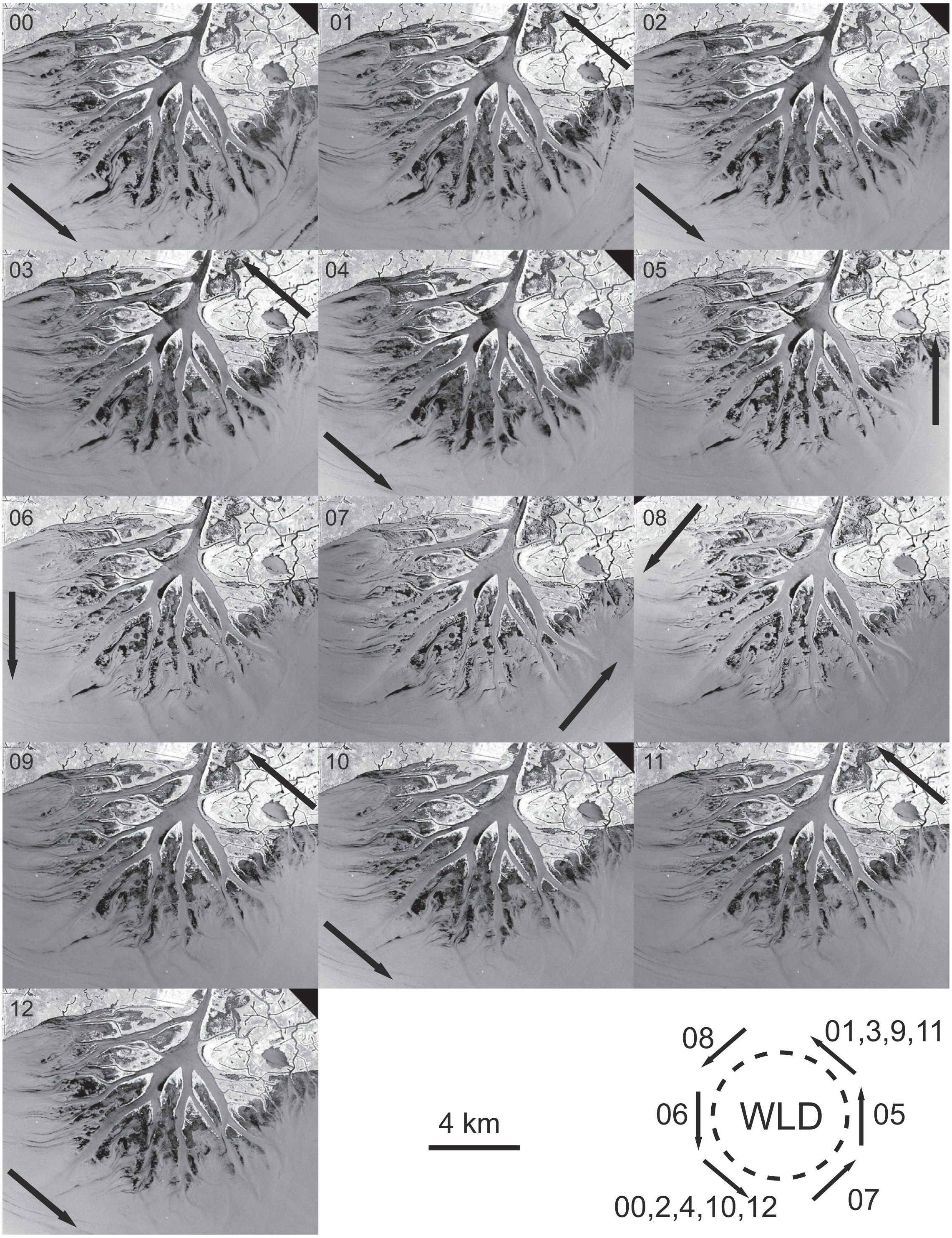

Fig. 2. SAR time-series. The thirteen UAVSAR images acquired on May, 8, 2015. The dark arrows indicate the flight heading/azimuth direction and the number refers to the image short ID (Table 2).

discharge at the WLD outlet was 4500 m^3/s as reported by the USGS station Wax Lake Outlet at Calumet, LA (ID:07381590, Latitude 29°41′52″, Longitude 91°22′22″) located about 20 km upstream of the WLD outlet. The large water discharge from WLD along with the discharge from Atchafalaya delta, located about 10 km to the east, make the delta area mostly freshwater (Holm and Sasser, 2001; Li et al., 2011). The entire WLD was inundated, meaning that the whole WLD surface was either emergent vegetation or water, without any land exposed (Fig. 1).

The sea surface elevation and wind data were measured at the Amerada Pass NOAA station (LAWMA, ID:8764227, Latitude 29°26.9′, Longitude 91°20.3′), which is located in the Atchafalaya Delta about 10 km east of WLD. We estimate that wind conditions at WLD and Atchafalaya are similar given the size of the landscape we are measuring and the flatness of the area. Between the first and last acquisition of the time-series, 2h50m apart during rising tide, the water height increased from 0.34 to 0.40 m with respect to the Mean Sea Level (MSL). During that same time span, the wind steadily increased from

Table 2
UAVSAR time-series acquired on May 8, 2015. The images are referred to by short ID in the text. UAVSAR is a left-looking instrument, so the look direction is 90° counterclockwise of the flight track heading. Flight heading is expressed in degrees from North, positive counterclockwise.

Full ID	Short ID	Time (UTC)	Flight heading
gulfco_14032_15057_000_150508_L090	00	11:20:46	220°
gulfco_32032_15057_001_150508_L090	01	11:34:05	40°
gulfco_14032_15057_002_150508_L090	02	11:48:29	220°
gulfco_32032_15057_003_150508_L090	03	12:01:14	40°
gulfco_14032_15057_004_150508_L090	04	12:15:44	220°
gulfco_00017_15057_005_150508_L090	05	12:29:12	0°
gulfco_18011_15057_006_150508_L090	06	12:43:11	180°
gulfco_05003_15057_007_150508_L090	07	12:56:50	310°
gulfco_23010_15057_008_150508_L090	08	13:10:33	130°
gulfco_32032_15057_009_150508_L090	09	13:27:55	40°
gulfco_14032_15057_010_150508_L090	10	13:41:23	220°
gulfco_32032_15057_011_150508_L090	11	13:53:50	40°
gulfco_14032_15057_012_150508_L090	12	14:09:07	220°

about 1.3 to 2.75 m/s blowing from the south-east direction with an average direction of 40° from north (positive counter-clockwise). Before the first acquisition the wind was blowing at about 1.3 m/s for 2–3 h, preceded by an approximate 12 h of 3.6 m/s winds continuing from the southeast direction. The wind anemometer is located at 11 m above MSL. The vegetation on the delta was blooming with dense production of both emergent and submerged biomass, which happened to be critical for estimating the current velocity from SAR on the delta. In the almost 3 h span between the first and last SAR acquisitions, the environmental conditions were reasonably steady such that we assume they were constant for our analysis.

4. Basic SAR observations and Doppler effect

4.1. SAR observations of WLD

The first acquired UAVSAR image (00) of WLD from May 8 is shown in Fig. 1. For illustrative purpose, the emergent vegetation is shown in green to highlight that most of the pattern complexities observed in the SAR image on the frontal part of the delta are in areas of open water. The classification between water and vegetation was done through intensity threshold using the HV polarization, which is more sensitive to vegetation than the other polarizations. Note that the threshold was adjusted for WLD proper and is not necessarily adequate outside of the delta as seen on the top-left of the image. Three main features are observed on the delta front, namely submerged channels, submerged vegetation, and biogenic slicks, as described in detail previously by Shaw et al. (2016b) and summarized below.

4.1.1. Submerged channels

At the downstream end of the river channels confined by emergent vegetation, the SAR images show the continuation of these channels underwater (yellow dots on Fig. 1), though the radar does not penetrate the water surface (Shaw et al., 2016b). Recent bathymetry surveys of WLD (Shaw and Mohrig, 2014) confirm that delta channels extend beyond emergent land boundaries and continue, submerged, into the bay for a few kilometers. These submerged channels stand out in the SAR image by having a uniform texture. They are at some places delineated with long dark/bright lines at the margins (mostly on the western side of the delta). These dark/bright lines are a well-known feature introduced during the SAR image processing and referred to as velocity bunching (Alpers et al., 1981; Lyzenga et al., 1985; Hasselmann and Hasselmann, 1991), which is briefly described in Section 4.2.1.

4.1.2. Submerged vegetation patches

The islands are the most complex in terms of variation in SAR intensity. Dark patches (blue dots on Fig. 1) are areas where underwater vegetation floats very close to the surface but does not break it (Fig. 3). This vegetation damps wind waves and creates a smooth water surface with low backscatter. These features, which could be confused with streaklines as they have similar low backscatter in the SAR, are stationary in time as opposed to biogenic slicks which migrate with current and wind. The water above the vegetation is static or moving much more slowly than the surrounding water due to the vegetation drag. Having interspersed static submerged vegetation patches in moving waters is the situation that allows us to extract surface current information from the measurement of SAR azimuth displacement, as explained in Section 5.

4.1.3. Biogenic streaklines

The dark streaklines observed in the SAR image (green dots on Fig. 1) are biogenic slicks (Huehnerfuss et al., 1983; Alpers and Huhnerfuss, 1989; Alpers and Espedal, 2004; Shaw et al., 2016b), which originate from the islands and surrounding wetlands. This natural material produced by the both emergent and submerged vegetation floats freely on the surface and becomes entrained by the currents and carried out to the bay while the source location remains static. The dynamic viscosity of the biogenic slick and the surface tension dampens small-scale wind waves, which in turn reduces the radar backscatter (e.g., Huehnerfuss et al., 1983). Biogenic slicks form into narrow bands through convergence within the flow and can serve as tracers of the

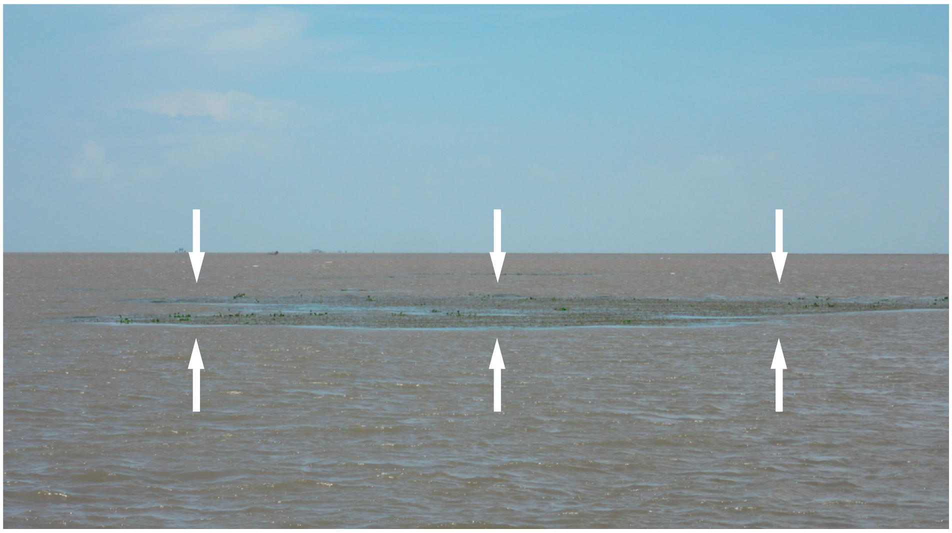

Fig. 3. Picture of a submerged vegetation patch on Wax Lake Delta (WLD). The submerged vegetation (white arrows) floating just beneath the water surface dampens small scale wind waves. The resulting smoother water patches alters the SAR backscatter and ultimately shows in the SAR image as dark, low backscatter patches. Note that this picture was taken in July 2015, which is later in the vegetation growing season compared to the UAVSAR acquisitions and shows vegetation that became emergent.

current general direction, as was confirmed by Shaw et al. (2016a) using current measurements. Potential wind drift must be taken into consideration when interpreting slick shape and orientation. We observe through the UAVSAR time-series both the migration and the fading of the streaklines (Fig. 2 and Supplementary Movie 1). Streakline migration during the time series of images, driven by a combination of current and wind, is in general visually unambiguous, but remains challenging to quantify due to lack of identifying features along a given streakline.

4.2. SAR azimuth displacement evidence

The azimuth displacement due to Doppler shift is a SAR effect which is related to the velocity of the ground target: the SAR image of a moving ocean surface "point" – whether due to swell, currents, or small waves forced by wind – will be displaced in the azimuth direction proportionally to its velocity and to the direction of motion relative to line-of-sight (e.g., Romeiser and Thompson, 2000). The SAR images over WLD display evidence of azimuth displacement both individually and relative to each other, as discussed below.

4.2.1. Azimuth displacement evidence on an individual image

A close-up view of azimuth displacement evidence is given on a subset of the SAR images in Fig. 4 (location given by the white square in Fig. 1). This subset area is located over a subaqueous channel. A static oil and gas platform is located approximately in the middle of the channel. Except for this platform, the entire image area shown is covered with water, with no emergent vegetation. The platform in the SAR image is easily identifiable from the high backscatter (bright area) (Fig. 4b and c). Backscatter from the water is less bright with no identifiable feature (grayish intensity), except in a few areas: (I) a bright/dark pair of lines that delineate the channel margins, (II) a dark area about 50 m away from the platform, and (III) some dark patches due to submerged vegetation (Fig. 4b). The bright/dark pair of lines are the result of velocity bunching, shown schematically in Fig. 4d, and is a manifestation of azimuth displacement in the presence of a surface current velocity varying in the along-track direction. On Fig. 4, profile A is drawn across the subaqueous channel. A schematic of the surface current is displayed on Fig. 4d, top graph. As the current velocity is varying along (A), the azimuth displacement amplitude is similarly varying, causing diverging or converging backscatter shift along the azimuth direction. This creates areas of low (dark) or high (bright) backscatter density (Fig. 4d, light shaded areas). Further evidence of azimuth displacement is the presence of the dark area (II). This dark area is not the shadow of the platform because the platform is too flat and the imaging angle too steep for it to occlude this area of the channel. Instead, it is related to the moving water as follows: the platform is surrounded by water moving approximately uniformly down-channel. The image of the moving water is displaced in SAR processing, leaving a dark spot, which we call "ghost spot" (not to be confused with azimuth or range ambiguities), where water at the location of the platform would have been imaged were the platform not present (Fig. 4d, dark shaded area). The distance between the platform and the ghost spot, i.e., S on Fig. 4b, is linearly related to the velocity of the surface water scatterers (surface waves) and flight azimuth.

4.2.2. Azimuth displacement evidence between images

Because the azimuth displacement occurs along the flight track direction, images acquired with different flight track directions display a relative shift between the locations of features subject to azimuth displacement. Detecting and quantifying this relative shift requires the geographically projected SAR images to be well co-registered. In our study, all emergent features are co-registered to a sub-pixel accuracy with no visible misregistration between the thirteen images of the time-series. Submerged vegetation patches and submerged channel signatures are also well co-registered between images acquired with the

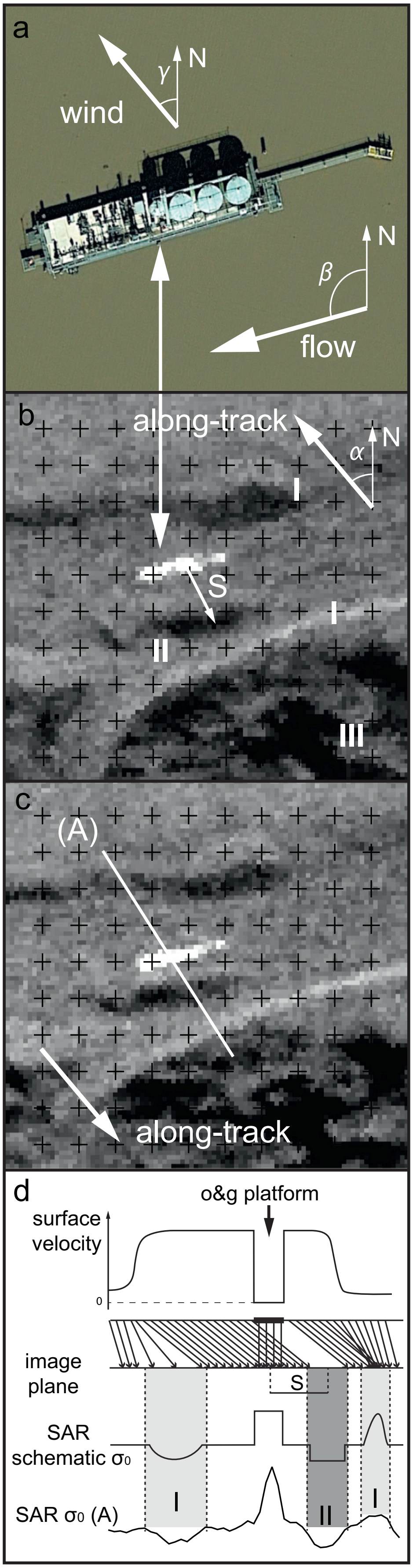

(caption on next page)

Fig. 4. Illustration of the azimuth displacement effect on WLD. a) Image of an oil & gas platform standing in a channel of WLD (white square, Fig. 1) (credit - Google Earth). b) SAR image (01) corresponding to the area. The bright patch indicates the platform backscatter. I, II, III indicate channel margin signatures from velocity bunching (light shade in panel d), platform backscatter ghost spot (dark shade in panel d; see 4.2.1), and submerged vegetation patches, respectively. S is the distance between the platform and its ghost spot. c) Same area as (b) but from another SAR acquisition (02) with anti-parallel flight track direction. d) Schematic of the azimuth displacement along profile A: schematic of the surface velocity in cross-track direction (first row); Azimuth displacement effect due to the moving surface (second row); schematic SAR σ_0 (third row); actual SAR σ_0 along profile A (fourth row). Note the good correspondence between the schematic image σ_0 and the actual SAR σ_0.

same along-track direction, i.e., between images 00, 02, 04, 10, 12, and between images 01, 03, 09, 11, respectively. The only differences between images from these two groups are wind gust signatures and streaklines that have migrated and/or faded between the respective times of acquisition. Between images acquired with different flight directions, either with opposite or crossing flight directions, emergent features retain accurate co-registration but submerged vegetation patches and submerged channel signatures appear to be shifted (misregistered) by up to 30 m, approximately. The shift offset is not the same between different pair of images, nor is it the same spatially over the delta for a given pair. Fig. 4b and c show the same area acquired from opposing imaging directions. The static platform is well coregistered between the two images. However, the shift between the platform and the ghost spot is different for the two images. Similarly, the positions of the dark/bright lines due to velocity bunching and corresponding to the channel margins visible in Fig. 4b and c, are not identical between the two images acquired from different directions. More generally, the submerged vegetation patches are also relatively shifted between each. As described in the next section, we make use of these measured Doppler-related shifts to derive surface currents within the WLD.

5. Theory for SAR imaging and Bragg scattering

5.1. Bragg scattering model

The backscatter from a water surface measured by SAR is related to the surface roughness. The common model to represent the ocean surface roughness is the 2-scale ocean surface model (e.g., Valenzuela, 1978). The first "scale" represents the small-scale roughness and is commonly modeled, under moderate wind condition, as Bragg scattering, where the dominant contributor to SAR backscatter are small-scale waves in the short gravity to capillary range. The second "scale" represents the long-wavelength, larger amplitude, swell type ocean waves, onto which the small-scale waves are riding.

In natural settings, the absolute Bragg waves velocity will be affected by multiple mechanisms, in particular the wind stress, underlying current, wave orbital motion, and Stokes drift (e.g., Alpers et al., 1981). Large-scale waves and the related Stokes drift, i.e., the second-scale model, are neglected in this study due to the shallow and calm sea conditions, especially within the vegetated regions. We therefore assume that the velocity of the advected ocean surface, $\vec{U}$, as sensed by the radar, is the vector sum of the Bragg wave free velocity, $\overrightarrow{U_B}$, the underlying current, $\overrightarrow{U_c}$, on which the Bragg waves are travelling, and the wind drift velocity, $\overrightarrow{U_w}$, as

$$\vec{U} = \overrightarrow{U_c} + \overrightarrow{U_B} + \overrightarrow{U_w} \tag{1}$$

Assuming a deep-water approximation, the Bragg waves free propagation velocity is equals to

$$U_B = \sqrt{g\lambda_B/2\pi} \tag{2}$$

with

$$\lambda_B = \lambda_R/2\sin\theta \tag{3}$$

λ_R, θ, g are the radar wavelength, incidence angle and gravitational acceleration, respectively. In linear wave theory, the deep-water approximation is generally accepted for depths that are greater than half the wavelength (Komar, 1976). Using the SAR specifications of Table 1 to estimate the Bragg wavelength, this corresponds to a depth between 7 and 12 cm over the range of UAVSAR incidence angles. This is sufficiently shallow to consider the approximation valid across the delta for the entire time-series based on bathymetry maps of the WLD (Shaw and Mohrig, 2014) and the calm observed sea state.

Given the uniform wind, flat topography, and absence of large wavelength waves on WLD, we can safely use the relation by Wu (1975), which states that Bragg wave's velocity attributable to the wind drift, $\overrightarrow{U_w}$,has the same direction as the wind that and its magnitude is approximately equal to 3% of the wind speed measured at 10 m elevation. We neglect potential nonlinearities due to wave-current interactions.

5.2. SAR Doppler shift

The azimuth displacement of a moving target is produced by the SAR processing algorithm applied to focus the image in the along-track direction. The displacement S in the along-track direction of a moving object relative to a stationary object at the same actual location is:

$$\vec{S} = -\frac{R}{V}(\vec{U}.\ \vec{r})\vec{a} \tag{4}$$

with R being the slant range (SAR antenna to target distance), V the aircraft speed, $\vec{U}$ the velocity of the scatterer, $\vec{r}$ a unit vector in the line-of-sight direction (pointing from the SAR antenna's phase center to the object on the ground), $\vec{a}$ the along-track unit vector, and "." representing the scalar product (dot product) of the vectors. $\vec{U}.\ \vec{r}$ represents the line-of-sight component of the scatterer velocity that is sensed by the radar.

5.3. Direction of Bragg waves

Although Bragg waves are wind generated, they are found to propagate in multiple directions (Holt, 2004). SAR backscatter is sensitive to Bragg waves that are migrating toward or away from the antenna. It is commonly accepted that any location on the surface simultaneously contains waves travelling in both directions. However, the amplitudes of the waves in the two directions are rarely identical, and therefore one component prevails in influencing the observed azimuth displacement. Poulter et al. (1994) observed from HF radar that under wind stress the Bragg waves that are travelling in the wind direction, or at least in a direction that is positive with respect to the wind direction, i.e., when $\overrightarrow{U_B}.\ \overrightarrow{V_w} > 0$ (where $\overrightarrow{V_w}$ is the wind unit vector), have larger amplitudes than the ones travelling against the wind. In this study we did not have access to the Doppler spectra of the SAR image to verify the increased spectral component at the frequency corresponding to positive orientation with respect to the wind. However, in the estimations of the current velocity presented below (Section 7), we observed that plausible values of current velocities were systematically obtained when assuming that dominant Bragg waves are moving positively with the wind direction. A situation arises for images 00, 01, 02, 03, 04, 09, 10, 11, and 12 where the line-of-sight directions are nearly orthogonal to the wind direction. The determination of the dominant Bragg wave direction in such situations is uncertain. The amplitudes of both waves could be similar, leading to Doppler splitting (Alpers et al., 1981), although in general other factors come into play, breaking that similarity. We observe from testing the two Bragg directions during estimations of the current velocities (Section 7) that the only possible direction of the

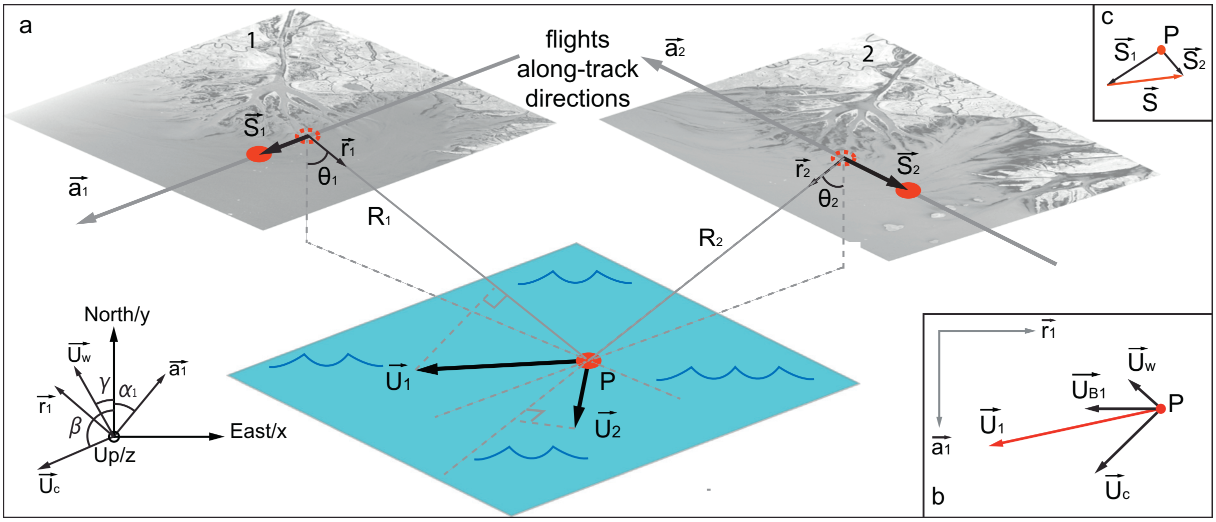

Fig. 5. Geometry of the multi flight tracks azimuth displacement effect. a) Schematic geometry of two SAR acquisitions with different flight track directions. $\vec{a_1}$, $\vec{r_1}$, θ_1, α_1 and $\vec{a_2}$, $\vec{r_2}$, θ_2, α_2 represent the azimuth (flight heading) unit vector, range (line-of-sight) unit vector, look angle, and azimuth angle with respect to North, for images 1 and 2, respectively (α_2 is not represented). $\vec{U_1}$ and $\vec{U_2}$ represent the water surface velocity sensed by the SAR antenna of images 1 and 2, respectively. The Doppler mechanism shifts the image of P by $\vec{S_1}$ and $\vec{S_2}$ in images 1 and 2, respectively. b) Representation of $\vec{U_1}$ which is modeled as the vectorial sum of the Bragg waves free velocity, $\vec{U_B}$, the underlying current, $\vec{U_c}$, and the wind drift, $\vec{U_w}$. The same principle applies to the definition of $\vec{U_2}$. $\vec{U_c}$ and $\vec{U_w}$ are the same regardless of the azimuth; $\vec{U_B}$, however, depends on the azimuth. γ and β represent the angles of $\vec{U_w}$ and $\vec{U_c}$ with respect to North, respectively. c) Image comparison using a pixel tracking algorithm determine the difference between azimuth displacements $\vec{S} = \vec{S_2} - \vec{S_1}$.

dominant Bragg waves that provides reasonable current velocity amplitude is the one that is moving in a direction positive with the current.

6. Application to an oil & gas platform

We estimate the surface velocity in the channel from the manual measurement of the shift S between the oil and gas platform and the ghost spot (Fig. 4) for SAR images 00, 01, 05, and 06, each presenting a different along-track direction or a different incidence angle. A manual measurement error of ± 1 pixel (± 5.5 m) is assumed for each estimate of S. The platform is located approximately in the middle of the channel. We assume the water flow direction in the vicinity of the platform to be approximately parallel to the channel margins. The flow orientation, β, with respect to North (positive counter-clockwise) is estimated to be 101°, and the wind direction, γ, is estimated to be blowing toward 40°. The flight heading is noted as α. With a geometry convention represented in Fig. 5, Eqs. (1) and (4) give:

$$\vec{S} = -\frac{R}{V}((\vec{U_c} + \vec{U_B} + \vec{U_w}).\ \vec{r})\vec{a} \tag{5}$$

which, when expressed in a right-handed Cartesian coordinate system with the x-axis directed east, the y-axis directed north, and the angles defined in Figs. 4 and 5, becomes:

$$-\frac{VS}{R} = U_c\begin{bmatrix}-\sin\beta\\ \cos\beta\\ 0\end{bmatrix}.\ \vec{r} + U_B\begin{bmatrix}-\cos\alpha\\ -\sin\alpha\\ 0\end{bmatrix}.\ \vec{r} + U_w\begin{bmatrix}-\sin\gamma\\ \cos\gamma\\ 0\end{bmatrix}.\ \vec{r} \tag{6}$$

with $\vec{r} = \begin{bmatrix}-\sin\theta\cos\alpha\\ -\sin\theta\sin\alpha\\ -\cos\theta\end{bmatrix}$, which reduces to

$$U_c = -\frac{1}{\sin(\beta-\alpha)}\left(\frac{VS}{R\sin\theta} + U_B + U_w\sin(\gamma-\alpha)\right) \tag{7}$$

with U_B given by (2) and U_w estimated from the anemometer measurement at Amerada Pass station (~2 m/s). Note that for $\alpha = \beta$, the current direction is perpendicular to the horizontal range and U_c cannot be determined.

Numerical values for the significant variables and estimates of surface currents for the four images are given in Table 3 along with the ADCP field measurements of the depth-average current acquired nearby the platform a few hours after the SAR acquisitions (see Table 3, Δt). The uncertainty in U_c, δU_c, is also calculated. Overall, the current magnitudes estimated from the azimuth displacement (average = 0.41 m/s) are close to the measured depth-average current (0.48 m/s). Estimates are consistently lower than measured current values but within the uncertainty range, except for image 01 which is a few cm/s outside the range.

7. Application to vegetation patches

The extraction of the in-channel current velocity from the azimuth displacement of the water using the oil and gas platform was useful for illustration purposes and for verifying that valid quantitative measurements could be made from shifts around stationary objects in a moving flow. The same technique can be applied more generally within the submerged delta islands, where similar imaging mechanisms are at work. The vegetation patches described in Section 4.1.2 are static and are surrounded by flowing water; and by analogy play the role of the oil and gas platform, with two major differences. First, the backscatter from the platform is very high (bright) making its differentiation from the ghost spot relatively easy. In contrast, vegetation patches and ghost spots backscatter intensities are similar, making it harder to identify and differentiate them. Second, the current magnitudes inside the submerged islands are smaller than in the channel, causing smaller azimuth displacement, i.e., a smaller offset distance between the vegetation patch and the ghost spot, to a point where the two may not be separated, but are overlapping.

Fig. 6a–b shows a close-up view of the area including a vegetation patch from two SAR images acquired with antiparallel flight directions (see also Supplementary Movie 2). Two intensity profiles are extracted at the same location across the vegetation patch in the along-track direction and plotted on Fig. 6c. We observe a slight shift between the two images due to the azimuth displacement. The mechanism is illustrated on Fig. 6c and is as follows: On the left side (along profile A) of the vegetation patch, the moving water (bright area) is shifted to the right, over the vegetation patch (dark area). On the right side of the vegetation patch, the moving water (bright area) is also shifted to the right,

Table 3
Estimation of the magnitude of the surface current, Uc, estimated from the azimuth displacement effect on the oil and gas platform. Estimates are close to the ADCP field measurement of the depth-averaged current made nearby the platform (0.48 m/s).

SAR Id	S (m)	R/V (s)	α (deg)	θ (deg)	U_B (m/s)	U_w (m/s)	U_c (m/ s)	δU_c	Δt (hour)
00	55	79.96	−139.9	51.96	−0.49	0.06	**0.44**	0.1	4.45
01	−77	114.15	40.3	57.52	0.47	0.06	**0.38**	0.06	4.23
05	−82.5	105.48	0.00	56.43	0.47	0.06	**0.43**	0.06	3.3
06	49.5	74.61	180.0	45.49	−0.51	0.06	**0.39**	0.1	3.53

away from the vegetation patch and leaving a ghost spot next to the (similarly dark) vegetation patch. Overall, the apparent shift to the right of both the left and right edges of the vegetation patch cause the plan shape of the patch to be approximately preserved (assuming similar flow velocity on both sides of the patch) and to appear shifted from its true location. The apparent shift (amplitude and direction) of the vegetation patches between two SAR images (S_1 and S_2 in Fig. 6c) will be different, depending on the SAR azimuth and direction of the moving surface. Difference in shape is attributed to possible wind change between acquisitions and the asymmetry of the SAR backscatter for Braggs waves travelling toward or away from the radar antenna. However, the shift difference, S, between S_1 and S_2 can be observed and quantified, and the current velocity can be estimated as explained below.

7.1. Feature shift measurement

Fig. 5 illustrates the acquisition geometry and shift due to the azimuth displacement. From two SAR images with different along-track directions, the relative shift $\vec{S}$ between the vegetation patches in the two images can be written as:

$$\vec{S} = \vec{S_2} - \vec{S_1} \tag{8}$$

with $\vec{S_1}$ and $\vec{S_2}$ representing the azimuth displacement from true position in images 1 and 2 respectively. Considering the along-track direction unit vectors $\vec{a_1}$ and $\vec{a_2}$ of images 1 and 2:

$$\vec{S} = S_2.\ \vec{a_2} - S_1.\ \vec{a_1} \tag{9}$$

or

$$\begin{bmatrix} S_x \\ S_y \end{bmatrix} = S_2 \begin{bmatrix} a_{2x} \\ a_{2y} \end{bmatrix} - S_1 \begin{bmatrix} a_{1x} \\ a_{1y} \end{bmatrix} \tag{10}$$

$S_x$and S_y are known from the measurement of the shift between the patches and the along-track directions $\vec{a_1}$ and $\vec{a_2}$ are known from the SAR acquisitions parameters. We can then determine S_1 and S_2 as long as the along-track directions are not collinear.

Eq. (6) can be written for image 1 as

$$\begin{bmatrix} U_{cx} \\ U_{cy} \\ 0 \end{bmatrix}.\ \vec{r_1} = -\frac{V_1 S_1}{R_1} - U_{B_1} \begin{bmatrix} -\cos\alpha_1 \\ -\sin\alpha_1 \\ 0 \end{bmatrix}.\ \vec{r_1} - U_w \begin{bmatrix} -\sin\gamma \\ \cos\gamma \\ 0 \end{bmatrix}.\ \vec{r_1}, \tag{11}$$

which can be simplified to:

$$U_{cx}\sin\theta_1\cos\alpha_1 + U_{cy}\sin\theta_1\sin\alpha_1 = \frac{V_1 S_1}{R_1} + (U_{B_1} + U_w\sin(\gamma - \alpha_1))\sin\theta_1 \tag{12}$$

Similarly, we can write eq. (6) for image 2 as

$$U_{cx}\sin\theta_2\cos\alpha_2 + U_{cy}\sin\theta_2\sin\alpha_2 = \frac{V_2 S_2}{R_2} + (U_{B_2} + U_w\sin(\gamma - \alpha_2))\sin\theta_2 \tag{13}$$

The planimetric components of the surface current velocity, U_{cx} and U_{cy}, can be solved using (12) and (13), giving the full 2D description of the surface current.

7.2. Dense surface velocity estimation

The estimation of the current velocity from (12) and (13) require S_1 and S_2, or equivalently S, to be estimated. The shifts, S, of submerged vegetation patches and submerged channel signatures on the delta islands are densely measured from pixel tracking. We use the Fourier-based correlation algorithm from COSI-Corr (Leprince et al., 2007). This algorithm uses a sliding window to estimate at each step the horizontal relative shift in the line and column direction between patches extracted from the SAR images. The shift maps obtained from the correlation can be directly converted to meters in the north/south and east/west directions because the SAR images are georeferenced. The correlation patches size is 128 × 128 pixels (~700 × 700 m), which reduces to an effective ~64 × 64 pixels (~350 × 350 m) due to the

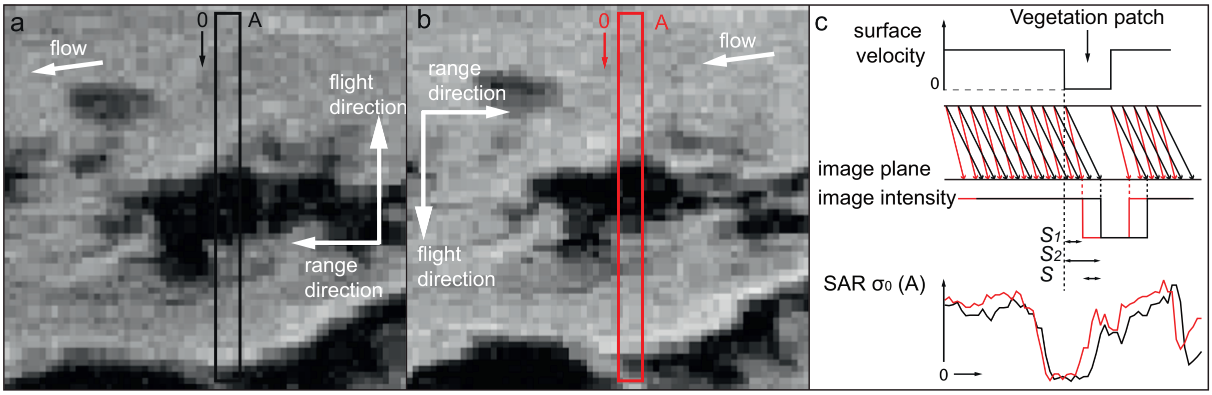

Fig. 6. Azimuth displacement of moving water measured using a static submerged vegetation patch. a) Subset of SAR image 05 over a vegetation patch. The water flow is almost collinear to the range direction. Backscatter intensity profile of box A is reported on panel (c), bottom plot. b) Same area as (a) but from SAR image 06 whose along-track direction is anti-parallel to SAR image 05. c) Schematic view of the azimuth displacement on submerged vegetation. Azimuth displacement schematics of profile A for images 05 and 06 are represented in black and red, respectively. The difference in geometry acquisitions causes the amplitude of the azimuth displacement between the two images to be different. The vegetation patches appears shifted between the two SAR images (see Section 7).

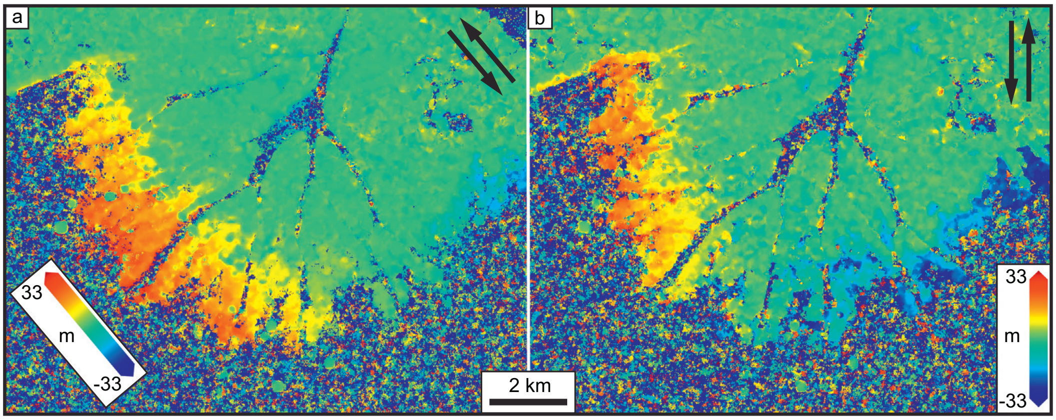

Fig. 7. Azimuth displacement measurement across the delta front. a) Map showing the shift amplitude, in meters, between features imaged in two SAR images with anti-parallel along-track directions (black arrows, upper right). The direction of the shift is given by the amplitude scale-bar orientation. Note that the shift has a constant direction over the entire footprint and corresponds to the along-track direction as expected from the theory of the azimuth displacement mechanism. Pixel tracking seaward of the delta front decorrelated due to the textureless backscatter in the open ocean. On emerged features (green area), the coregistration of the SAR images is very good and centered at 0. b) Same as (a) but with another pair of SAR images.

strong bell-shaped weighting of the patches to avoid Fourier transform artifacts. Such a large size was necessary to reduce measurement noise due to the SAR speckle noise and the non-uniform distribution of the vegetation patches. Examples of relative shift maps obtained between pairs of images are given in Fig. 7.

In the analysis, twelve pairs are formed between non-collinear along-track directions SAR images. For each pair, vegetation patch shifts are measured from pixel tracking as described above. Images 00, 02, 04, 10, 12 (“group 1”) and 01, 03, 09, 11 (“group 2”) have the same along-track directions and do not present any difference except for biogenic slick migration and some wind gust effects; all vegetation patches are precisely co-registered. Therefore, no additional information is obtained by comparing each of these images to other ones of the time-series. However, to take advantage of the redundant information contained in each group, we do a principal component analysis (PCA) on each group and keep the first component as a unique representation for the respective group, named 00group and 01group. The PCA reduces the speckle noise inherent to SAR imagery, and reduces the amplitude of the changing features slick and wind gust signature. The benefit is an increased correlation quality with reduced outliers. The 12 pairs correspond to the possible pairings between 00group, 01group, 05, 06, 07, and 08 (without collinear pairing, i.e., 00group and 01group, 05 and 06, and 07 and 08).

Areas outside the submerged islands such as channels and the delta front are discarded from the shift maps. Similarly, areas close to emergent vegetation are discarded because the strong backscatter from the static emergent vegetation bias the measurement toward zero. Spurious measurements were also filtered out. Each of the twelve cleaned shift maps are used to solve for U_{cx} and U_{cy}. A median U_{cx} and U_{cy} is then obtained from the twelve estimations. A vector representation of the median estimated current velocity is represented in Fig. 8 (yellow arrows).

8. Discussion

8.1. Measurement validity and consistency

The orientation and amplitude of the current is qualitatively consistent with expectation based on the delta morphology and our current understanding of delta dynamics determined from field studies of the Wax Lake Delta: water brought on the delta from the channels spreads laterally to the islands and finally drains out to sea at the delta front (Hiatt and Passalacqua, 2015; Shaw et al., 2016a). The average current amplitude on the islands is about 11 cm/s, with a standard deviation of 5 cm/s, and 95% of measurements show currents < 20 cm/s.

The orientation and amplitude of the current is also generally consistent with the ADCP field survey which was located 1–2 km downstream (red vectors in Fig. 8). In the eastern portion of the delta, the estimated current orientation is at odds with the orientation of the current from the boat survey located downstream where the ADCP is measuring a southwesterly flow direction. This apparent current orientation mismatch is interpreted as the product of an alongshore current in front of the delta, as indicated by the streakline patterns (Fig. 1).

Three out of four water current velocity estimations inside a channel derived from the oil and gas platform ghost spot (Section 6 and Table 3) matched within error the nearby ADCP measurement. Although the current velocity estimation method applied to the platform is different from the method applied to the vegetation patches, the underlying SAR imaging model is identical, i.e., surface scatterer velocity sensed by the SAR is modeled as the simple vector sum of the Bragg waves free velocity, the underlying current, and wind drift, which validates to first order the model of the ocean surface used in this study.

Some of the biogenic slicks were manually tracked in the SAR time-series using persistent and identifiable heterogeneities in the slick (green dots and cyan vectors in Fig. 8) (Supplementary Movie 1). On the delta front, the surface velocity orientation and amplitude derived from the streaklines are consistent with nearby ADCP measurements. There were only two slick velocity measurements that could be done inside the islands. Measurement M1 (Fig. 8) is located in the middle of the island, toward the seaward end, away from vegetation patches. The derived amplitude of the current (24 cm/s) is consistent in amplitude with the velocity amplitude derived from azimuth displacement in a nearby area. The orientation, however, is different. This is possibly explained by the probable reorientation of the current in the middle of the island toward the southwest. The second misfit slick velocity measurement inside an island (M2 in Fig. 8) has an amplitude consistent with estimates from the azimuth displacement in the vicinity, but with an orientation at odds with nearby current estimate, especially with the velocity derived from the vegetation patch bordering the eastward channel. This discrepancy possibly arises from violation of the assumption that flows around opposite sides of a vegetation patch are approximately identical in amplitude and direction. The strong channel flow southward on the east side of the patch differs from the slower westward flow (measured from biogenic slick tracking) on the west side of the patch.

Despite overall good qualitative validation, further quantitative validation of the current flow on submerged islands is necessary.

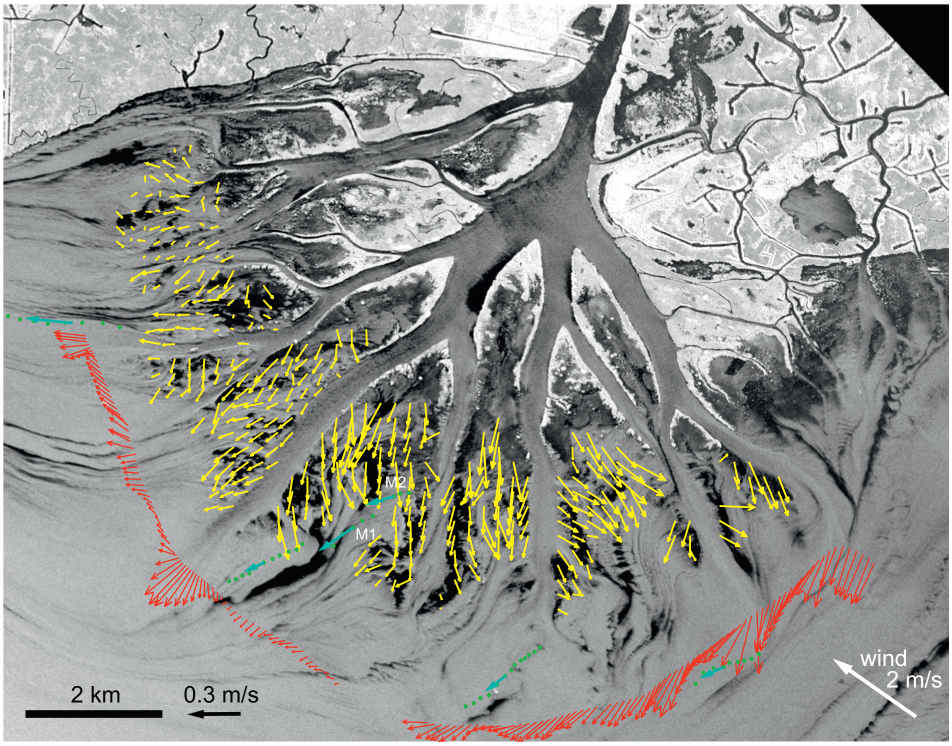

Fig. 8. 2-dimensional water current estimated from SAR on the submerged deltaic islands. Yellow vectors indicate the orientation and amplitude of the median water current estimated from the multi-pass SAR imagery. Estimates of the water current velocity could only be obtained in areas containing submerged vegetation that enable the measurement of the azimuth displacement related to the surface velocity of water flowing around the vegetation. Red vectors (same as in Fig. 1) indicate water current measured in an ADCP field survey within hours of the SAR acquisitions. Green dots are successive positions of biogenic slick features manually tracked in the SAR time-series, with the average current amplitude and direction represented by cyan arrows.

8.2. Method limitation

The first source of bias and error in our approach relates to the azimuth displacement measurement from the pixel tracking algorithm: 1) In situations where the biogenic slicks present sharp contours and larger heterogeneities, the tracking algorithm could track the slick migration instead of the azimuth displacement. In this study the fading and smooth shape of the streaklines did not provide the necessary texture for this to be done. 2) The strong backscatter of an emergent structure inside a correlation patch could bias ("locking" effect) the measurement toward zero. 3) The method assumes the shape of the feature, in our case the shape of a vegetation patch, to be similar between all compared SAR images. This assumption can be wrong depending on wind and current conditions around the patches. An example can be seen on Fig. 6 where the shape of the middle vegetation patch is not rigorously identical.

The second source of error relates to the SAR model used to estimate the current from the azimuth displacement: 1) Slight errors in the antenna position and orientation telemetry could bias the location of the backscatter in the SAR image. This source of error is also critical in the Doppler anomaly analysis method described by Chapron et al. (2005) using satellite SAR imagery. 2) Simplifying assumptions in the model such as the absence of current-wave and current-wind interactions, and the use of a simple Bragg scattering model are other sources of error. The systematic slight underestimation of the current in the oil and gas platform case, for instance, might be due to simplifications of this model.

Regarding acquisition practicality, this approach requires at least two images acquired with non-collinear flight headings, similar to the ATI and Doppler shift anomaly analysis. Orthogonal along-track directions provide optimal geometrical constraints but are subject to stronger backscatter difference, leading to noisier correlation. The images must also be acquired within a short time-span to reduce changes in environmental conditions, which are assumed to be constant. These constraints can be satisfied with an airborne system, but are out of reach for spaceborne SAR. The approach relies also on the presence of interspersed, low-backscatter, static features relative to which one measures the azimuth displacement. On WLD, these features were submerged vegetation patches, whose presence is seasonal only. UAVSAR images of the WLD acquired during the winter months when the biomass production is limited do not show any submerged vegetation, which precludes application of this measurement technique inside the islands during that time. We note that these static features do not have to be vegetation nor do they have to be in shallow waters.

8.3. Flow pattern

The difference of water velocities between the fast-flowing water in the channel (~40 cm/s) and the slower flow in the submerged islands (~10–20 cm/s) is consistent with previous field observations (Shaw et al., 2016a). This is also consistent with the interpretation of the islands being depositional where entrained sediments are dropped from the water as it slows down within the islands. Overall, we observe that water flows from the channels to the islands and then is drained out to the delta front. As the water moves out from the islands it merges with the westward flow along the delta front, and is possibly further slowed down by the incoming rising tide present at the times of the UAVSAR acquisitions.

Over the delta, the pattern of water current velocity can be complex and can change abruptly. ADCP measurements show rapid increase of the water velocity in the subaqueous part of the channels (Shaw and Mohrig, 2014). A general trend of water velocity decrease in the islands is observed from east to west. Current orientation can also change abruptly. The streakline-derived current directions on the eastern delta are approximately perpendicular to the ADCP measurements just a few hundred meters northward (Fig. 7). The same observation of rapid current orientation change is made inside the island where streakline-derived current estimates were made. We also suggest that large submerged vegetation patches can affect the nearby current by diverting part of the flow around them.

Overall the inferred current velocity direction and amplitude are in agreement with expectations based on the delta morphology. The rapidness of spatial current changes reveals the complexity of flow in deltaic areas, and SAR-derived velocity patterns could be a powerful tool to understand water routing of sediment, carbon and solutes across river deltas.

9. Conclusions

In this study we describe a new method for estimating flow fields in shallow water using SAR, and apply it to estimate the current velocity over shallow deltaic islands in the Wax Lake Delta of coastal Louisiana from a series of L-band airborne SAR images acquired every 15–20 min for 3 h with various flight directions. The correlation of the spatially registered SAR images reveals apparent misregistration of several meters on the submerged delta front that are attributed to the Doppler-induced azimuth displacement due to the velocity of the water surface. Using a simple Bragg scattering model and considering independent contributions of the Bragg waves free velocity, wind drift, and underlying current to the azimuth displacement, the current velocities inside submerged islands on the delta are estimated. The technique also is validated locally where current estimate from the azimuth displacement made visible by a static oil & gas platform in the middle of a major channel of the delta is within expected errors from concurrent and collocated ADCP field measurement (Table 3).

The derived SAR-based surface currents agree well with in situ currents measured offshore in relative proximity to the SAR-derived currents. The measured currents shows that water spreads laterally from the main deltaic channels and converges within the submerged, vegetated deltaic islands. Current velocities within the submerged islands were ~0.2 m/s, or approximately half the speed of channelized currents, consistent with shallow depths (< 1 m) and enhanced flow resistance caused by vegetation. The method presented here is subject to several limitations and simplifying assumptions and would benefit from additional quantitative validation. Despite these limitations, the demonstrated approach is novel in terms of estimating the current from Doppler-induced azimuth displacement and shows interesting potential for remotely measuring spatially extensive current fields in a shallow deltaic environment, filling a gap in measurements that are extremely difficult to make on the ground. Given the importance of water flow velocity within deltaic islands for land building, carbon storage, and biogeochemical cycling, any method that enables estimation in those areas is of value, and can be of use to improve hydrological models and, in a practical application, for projects addressing coastal resilience and sustainability.

Supplementary data to this article can be found online at https://doi.org/10.1016/j.rse.2018.04.035.

Acknowledgments and Data

The research described in this paper was funded by the California Institute of Technology, and the Jet Propulsion Laboratory, under a contract with the National Aeronautics and Space Administration, and with additional support from a NSF FESD Delta Dynamics Collaboratory grant (EAR-1135427) and a NSF postdoctoral grant (EAR-1250045). The UAVSAR data are courtesy of NASA Jet Propulsion Laboratory/California Institute of Technology and are openly available at https://www.asf.alaska.edu. Raw boat survey data are available for download in Supplementary Material. The authors thank the boat survey crew Daniel D. Duncan, Max S. Daniller-Varghese, and Daniel Aylward, and the UAVSAR team for their help in acquiring these datasets. Mention of trade names or commercial products is not an endorsement or recommendation for use by the U.S. Government.

References

Allen, Y.C., Couvillion, B.R., Barras, J.A., 2012. Using multitemporal remote sensing imagery and inundation measures to improve land change estimates in coastal wetlands. Estuar. Coasts 35 (1), 190–200. http://dx.doi.org/10.1007/s12237.011.9437.z.

Alpers, W., Espedal, H.A., 2004. Oils and Surfactants. In: Jackson, C.R., Apel, J.R. (Eds.), Synthetic Aperture Radar Marine User's Manual. U.S. Department of Commerce, Washington, DC, pp. 263–275.

Alpers, W., Hennings, I., 1984. A theory of the imaging mechanism of underwater bottom topography by real and synthetic aperture radar. J. Geophys. Res. Oceans 89 (10), 529–10,546.

Alpers, W., Huhnerfuss, H., 1989. The damping of ocean waves by surface films: a new look at and old problem. J. Geophys. Res. Oceans 94, 6251–6265.

Alpers, W., Ross, D.B., Rufenach, C.L., 1981. On the detectability of ocean surface waves by real and synthetic aperture radar. J. Geophys. Res. Oceans Atmos. 86 (C7), 6481–6498. http://dx.doi.org/10.1029/JC086iC07p06481.

Carle, M.V., Sasser, C.E., Roberts, H.H., 2015. Accretion and vegetation community change in the Wax Lake Delta following the historic 2011 Mississippi river flood. J. Coast. Res. 31 (3), 569–587. http://dx.doi.org/10.2112/JCOASTRES-D-13-00109.1.

Chapman, R.D., Gotwols, B.L., Sterner II, R.E., 1994. On the statistics of the phase of microwave backscatter from the ocean surface. J. Geophys. Res. 99 (C8), 16,293–16,301.

Chapron, B., Collard, F., Ardhuin, F., 2005. Direct measurements of ocean surface velocity from space: interpretation and validation. J. Geophys. Res. Oceans 110, C07008. http://dx.doi.org/10.1029/2004JC002809.

Fore, A.G., Chapman, B.D., Hawkins, B.P., Hensley, S., Jones, C.E., Michel, T.R., Muellerschoen, R.J., 2015. UAVSAR plarimetric calibration. IEEE Trans. Geoscience and Remote Sensing 53 (6), 3481–3491. http://dx.doi.org/10.1109/TGRS.2014.2377637.

Galloway, W.E., 1975. Process framework for describing the morphologic and stratigraphic evolution of deltaic depositional systems. In: Broussard, M.L. (Ed.), Deltas Models for Exploration. Houston Geological Societypp. 87–98.

Geleynse, N., Hiatt, M., Sangireddy, H., Passalacqua, P., 2015. Identifying environmental controls on the shoreline of a natural river delta. J. Geophys. Res. Earth Surf. 120 (5), 877–893.

Goldstein, R.M., Zebker, H.A., 1987. Interferometric radar measurement of ocean surface current. Nature 328, 707–709.

Goldstein, R.M., Barnett, T.P., Zebker, H.A., 1989. Remote-sensing of ocean currents. Science 246 (4935), 1282–1285. http://dx.doi.org/10.1126/science.246.4935.1282.

Graber, H.C., Thompson, D.R., Carande, R.E., 1996. Ocean surface features and currents measured with synthetic aperture radar interferometry and HF radar. J. Geophys. Res. 101 (C11) (25 813–25 832).

Hasselmann, K., Hasselmann, S., 1991. On the nonlinear mapping of an ocean wave spectrum into a synthetic aperture radar image spectrum and its inversion. J. Geophys. Res. 96 (C6), 10713–10729. http://dx.doi.org/10.1029/91JC00302.

Hiatt, M., Passalacqua, P., 2015. Hydrological connectivity in river deltas: the first-order importance of channel-island exchange. Water Resour. Res. 51 (4), 2264–2282.

Holm, G.O., Sasser, C.E., 2001. Differential salinity response between two Mississippi river subdeltas: implications for changes in plant composition. Estuar. Coasts 24 (1), 78–89.

Holt, B., 2004. SAR Imaging of the Ocean Surface. In: Jackson, C.R., Apel, J.R. (Eds.), Synthetic Aperture Radar Marine User's Manual. U.S. Department of Commerce, Washington, DC, pp. 263–275.

Huehnerfuss, H., Alpers, W., Garrett, W.D., Lange, P.A., Stolte, S., 1983. Attenuation of capillary and gravity waves at sea by monomolecular organic surface films. J. Geophys. Res. Oceans 88, 9809–9816.

Johannessen, J.A., Chapron, B., Collard, F., Kudryavtsev, V., Mouche, M., Akimov, D., Dagestad, K.F., 2008. Direct ocean surface velocity measurements from space: improved quantitative interpretation of Envisat ASAR observations. Geophys. Res. Lett. 35 (22). http://dx.doi.org/10.1029/2008GL035709.

Kolker, A.S., Li, C.Y., Walker, N.D., Pilley, C., Ameen, A.D., Boxer, G., Ramatchandirane, C., Ullah, M., Williams, K.A., 2014. The impact of the great Mississippi/Atchafalaya river flood on the oceanography of the Atchafalaya shelf. In: Continental Shelf Research. 86. pp. 17–33. http://dx.doi.org/10.1016/j.csr.2014.04.023.

Komar, P.D., 1976. The generation of waves and their movement across the sea. In: Komar, P.D. (Ed.), Beach processes and sedimentation, Second Edition. Prentice Hall, Upper Saddle River, pp. 263–275.

Kudryavtsev, V., Myasoedov, A., Chapron, B., Johannessen, J.A., Collard, F., 2012. Imaging mesoscale upper ocean dynamics using synthetic aperture radar and optical data. J. Geophys. Res. 117, C04029. http://dx.doi.org/10.1029/2011JC007492.

Leprince, S., Barbot, S., Ayoub, F., Avouac, J.-P., 2007. Automatic and precise orthorectification, coregistration, and subpixel correlation of satellite images, application to ground deformation measurements. IEEE Trans. Geosci. Remote Sens. 45 (6), 1529–1558.

Li, C., Roberts, H., Stone, G.W., Weeks, E., Luo, Y., 2011. Wind surge and salt-water intrusion in Atchafalaya Bay during onshore winds prior to cold front passage. Hydrobiologia 658 (1), 27–39. http://dx.doi.org/10.1007/s10750.010.0467.5.

Lodge, D.W.S., 1983. Surface expressions of bathymetry on Seasat synthetic aperture radar images. Int. J. Remote Sens. 4, 639–653.

de Loor, G.P., 1981. The observation of tidal patterns, currents, and bathymetry with SLAR imagery of the sea. IEEE J. Ocean. Eng. 6, 124–129.

Lyzenga, D.R., Shuchman, R.A., 1982. Synthetic aperture radar measurements of ocean surface currents. Geophys. Res. Lett. 9 (7), 747–750.

Lyzenga, D.R., Shuchman, R.A., Lyden, J.D., Rufenach, C.L., 1985. SAR imaging of waves in water and ice: evidence for velocity bunching. J. Geophys. Res. 90, 1031–1036.

Madsen, S.N., 1989. Estimating the doppler centroid of SAR data. IEEE Trans. Aerosp. Electron. Syst. 25 (2), 134–140.

Morton, R.A., Bernier, J.C., 2010. Recent subsidence-rate reductions in the Mississippi Delta and their geological implications. J. Coast. Res. 555–561. http://dx.doi.org/10.2112/JCOASTRES-D-09-00014R1.1.

Olliver, E.A., Edmonds, D.A., 2017. Defining the ecogeomorphic succession of land building for freshwater, intertidal wetlands in Wax Lake Delta, Louisiana, Estuarine. Coast. Shelf Sci. 196, 45–57. http://dx.doi.org/10.1016/j.ecss.2017.06.009.

Orton, G.J., Reading, H.G., 1993. Variability of deltaic processes in terms of sediment supply, with particular emphasis on grain size. Sedimentology 40 (3), 475–512.

Paduan, J.D., Rosenfeld, L.K., 1996. Remotely sensed surface currents in Monterey Bay from shore-based HF radar (Coastal Ocean Dynamics Application Radar). J. Geophys. Res. Oceans 101 (C9), 20,669–20,686.

Poulter, E.M., Smith, M.J., McGregor, J.A., 1994. Microwave backscatter from the sea surface: Bragg scattering by short gravity waves. J. Geophys. Res. Oceans 99 (C4), 7929–7943.

Roberts, H.H., DeLaune, R.D., White, J.R., Li, C., Sasser, C.E., Braud, D., Weeks, E., Khalil, S., 2015. Floods and cold front passages: impacts on coastal marshes in a river diversion setting (wax Lake delta area, Louisiana). J. Coast. Res. 31 (5), 1057–1068.

Romeiser, R., Alpers, W., 1997. An improved composite surface model for the radar backscattering cross section of the ocean surface, 2, Model response to surface roughness variations and the radar imaging of the underwater bottom topography. J. Geophys. Res. Oceans 102 (25), 251–25,267.

Romeiser, R., Thompson, D.R., 2000. Numerical study on the along-track inteferometric radar imaging mechanisms of oceanic surface currents. IEEE Trans. Geosci. Remote Sens. 38, 446–458.

Romeiser, R., Breit, H., Eineder, M., Runge, H., Flament, P., de Jong, K., Vogelzang, J., 2005. Current measurements by SAR along-track interferometry from a space shuttle. IEEE Trans. Geosci. Remote Sens. 43, 2315–2324.

Romeiser, R., Runge, H., Suchandt, S., Sprenger, J., Weilbeer, H., Sohrmann, A., Stammer, D., 2007. Current measurements in rivers by spaceborne along-track InSAR. IEEE Trans. Geosci. Remote Sens. 45, 4019–4030 (2007).

Shaw, J.B., Mohrig, D., 2014. The importance of erosion in distributary channel network growth, Wax Lake Delta, Louisiana, USA. Geology 42 (1), 31–34. http://dx.doi.org/10.1130/G34751.1.

Shaw, J.B., Mohrig, D., Wagner, W.R., 2016a. Flow patterns and morphology of a prograding river delta. J. Geophys. Res. Earth Surf. 121. http://dx.doi.org/10.1002/2015JF003570.

Shaw, J.B., Ayoub, F., Jones, C.E., Lamb, M.P., Holt, B., Wayne Wagner, R., Coffey, T.S., Austin Chadwick, J., Mohrig, D., 2016b. Airborne radar imaging of subaqueous channel evolution in Wax Lake Delta, Louisiana, USA. Geophys. Res. Lett. 43, 5035–5042. http://dx.doi.org/10.1002/2016GL068770. 2016GL068770.

Syvitski, J.P., Saito, Y., 2007. Morphodynamics of deltas under the influence of humans. Glob. Planet. Chang. 57 (3–4), 261–282. http://dx.doi.org/10.1016/j.gloplacha.2006.12.001.

Temmerman, S., Bouma, T.J., Govers, G., Wang, Z.B., De Vries, M.B., Herman, P.M.J., 2005. Impact of vegetation on flow routing and sedimentation patterns: three-dimensional modeling for a tidal marsh. J. Geophys. Res. Earth Surf. 110 (F4), F04019. http://dx.doi.org/10.1029/2005JF000301.

Tessler, Z.D., Vorosmarty, C.J., Grossberg, M., Gladkova, I., Aizenman, H., Syvitski, J.P.M., Foufoula-Georgiou, E., 2015. Profiling risk and sustainability in coastal deltas of the world. Science 349 (6248), 638–643. http://dx.doi.org/10.1126/science.aab3574.

Valenzuela, G.R., 1978. Theories for the interaction of electromagnetic and ocean waves – a review. Bound.-Layer Meteorol. 13 (1–4), 61–85.

Wu, J., 1975. Wind-induced drift current. J. Fluid Mech. 68 (49–7).